

pubs.acs.org/journal/apchd5 Article

# Chiral Optical Properties of Plasmonic Kagome Lattices

Xitlali G. Juarez, Francisco Freire-Fernández, Siamak Khorasani, Marc R. Bourgeois, Yi Wang, David J. Masiello, George C. Schatz, and Teri W. Odom\*



Cite This: ACS Photonics 2024, 11, 673-681



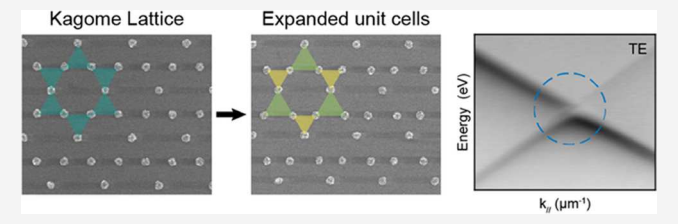
**ACCESS** I

Metrics & More

Article Recommendations

Supporting Information

**ABSTRACT:** Kagome lattices can be considered hexagonal lattices with a three-nanoparticle unit cell whose symmetry may lead to the formation of higher-order topological states. This work reports the emergence of polarization-dependent features in the optical band structures of plasmonic Kagome lattices through lattice engineering. By expanding the separations between particles in a unit cell while preserving lattice spacing, we observed additional modes at the *K*-points of aluminum nanoparticle



Kagome lattices. As the rotational symmetry was reduced from 6- to 3-fold, a splitting at the *K*-point was observed as well as the presence of an additional surface lattice resonance (SLR) band under linear polarization. This SLR band also exhibited a chiral response that depended on the direction of circularly polarized light and resulted in asymmetry in the optical band structure. The polarization-dependent response of plasmonic Kagome lattices can inform the design of systems that support topological states at visible wavelengths.

KEYWORDS: lattice plasmons, surface lattice resonance, Kagome lattice, circularly polarized light, plasmonic nanoparticle lattice, topological photonics

### **■ INTRODUCTION**

Photonic topological insulators are materials that are insulating in their bulk but conducting at their interfaces because of topological edge states that enable the robust, unidirectional propagation of photons. 1,2 Edge states can form at the interface between two topologically distinct regions from the bulkboundary correspondence.3 The first experimental demonstration of photonic topological edge states required an external magnetic field to break time-reversal symmetry in order to form topological nontrivial phases, which limited operational wavelengths to the microwave regime where magneto-optical effects are strong.<sup>4</sup> An alternative approach has also produced edge states by lattice-symmetry engineering, such as deforming the unit cells of honeycomb lattices. In this method, a honeycomb lattice is treated as a hexagonal lattice with hexamer unit cells, and as the hexamer unit cell is either shrunk or expanded, topologically trivial or nontrivial band gaps, respectively, can emerge at the  $\Gamma$ -point. When topologically distinct lattices are situated adjacent to each other, a pair of helical edge states can form at the interface and be accessed individually using circularly polarized light.<sup>6</sup> Manipulating the lattice symmetry of honeycomb lattices has generated topological states for diverse applications, including the unidirectional transport of photons,<sup>7</sup> exciton—polaritons,<sup>8</sup> phonon—polaritons,<sup>10</sup> and topological lasing.<sup>11,12</sup>

Kagome lattices have also received attention because they can support higher-order topological states. <sup>13,14</sup> In addition to topological edge states (1D) at their *K*-points, Kagome lattices can also exhibit corner modes (0D) at the physical corners of

finite structures due to near-field and far-field interactions between the unit cells. 15 Similar to those in honeycomb lattices, topological modes in a Kagome lattice form when the trimer unit cells of the hexagonal lattice are either shrunk (trivial) or expanded (nontrivial). Shrunken or expanded unit cells result in a reduction of the rotational symmetry of the lattice from 6- to 3-fold, and a band gap at the K-point opens due to hybridization and avoided crossings of formerly degenerate bands. 14,16 Edge states also emerge at the interface between trivial and nontrivial lattices and corner modes at the corners of heterostructures. 14-16 Although topological states have been experimentally demonstrated in honeycomb and Kagome lattices 15,17-19 across the electromagnetic spectrum, the propagation of photons along edge states is reduced in the visible regime. The limitations are due to the large absorption losses of materials used to fabricate topological photonic systems, such as silicon<sup>20,21</sup> and SiN<sub>x</sub>.

Plasmonic nanoparticle (NP) lattices offer an approach to realize topological states at visible wavelengths by engineering their surface lattice resonances (SLRs). SLRs form through hybridization of the localized surface plasmons (LSPs) of

Received: October 19, 2023 Revised: January 8, 2024 Accepted: January 8, 2024 Published: January 30, 2024





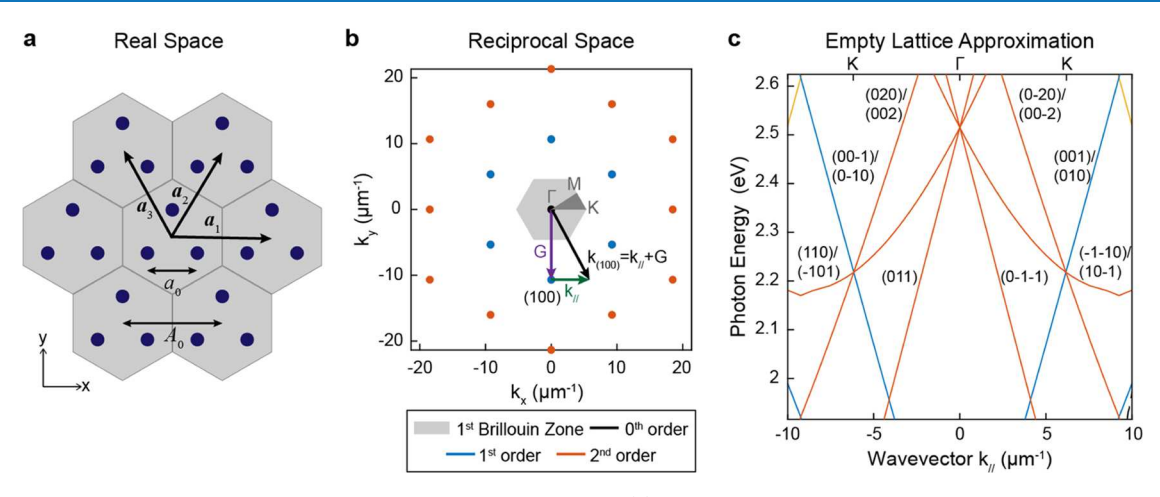


Figure 1. Designing a Kagome lattice using the empty lattice approximation. (a) Scheme of a Kagome lattice with lattice spacing  $A_0$  and unit-cell spacing  $a_0$ . The real space vectors of the lattice are denoted as  $a_1$ ,  $a_2$ , and  $a_3$ . The gray hexagons indicate the trimer arrangement of NPs in the unit cells and periodicity of the lattice. (b) Reciprocal space of the Kagome lattice. The 1st Brillouin zone and the high symmetry points of the lattice are indicated in gray. The reciprocal lattice vector,  $G_{(ijk)}$ , is shown in purple, while the in-plane wavevector  $k_{//}$  is indicated in green. The vector corresponding to the diffractive order of the lattice is represented as  $k_{(ijk)}$ . Blue and orange dots indicate the 1st and 2nd diffractive orders. (c) Empty lattice dispersion for  $A_0 = 680$  nm and n = 1.45 along the Γ-K direction.

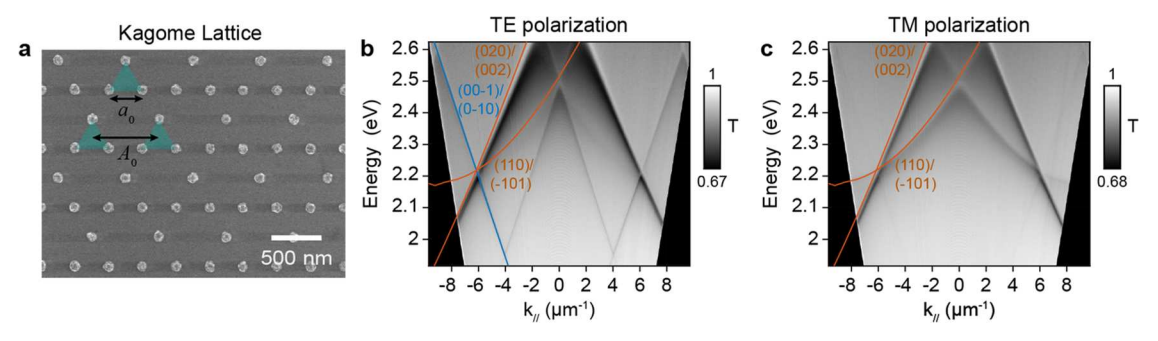


Figure 2. Photonic band structure of an Al Kagome lattice. (a) Scanning electron microscopy (SEM) image of a fabricated lattice with Al NPs (d = 100 nm, h = 50 nm). The blue triangles indicate the trimer arrangements of the NPs in the unit cells of the lattice. Measured photonic band structure of fabricated Al Kagome lattices under (b) TE-polarized and (c) TM-polarized light along Γ-K. The calculated diffractive modes (blue and orange lines) are overlaid on the left side of the measurements in panels (b, c).

individual NPs to the diffractive modes of the lattice. The inphase oscillations of the NPs reduce radiative losses while supporting strong, localized electric fields around the NPs. 22-24 Theory has predicted that non-Bravais plasmonic lattices (i.e., lattices with nonprimitive unit cells consisting of at least two particles) can form topological edge states at different band edges as well as at high symmetry points.<sup>25-29</sup> Moreover, such lattice symmetries exhibit complex near-field characteristics from interactions between multiparticle unit cells.<sup>30,31</sup> For example, honeycomb lattices treated as 2-NP unit cells on a hexagonal lattice<sup>32</sup> and square lattices with multiparticle unit cells<sup>33</sup> exhibit SLR modes from the hybridization of inequivalent LSPs. In addition, the arrangement of particles within a unit cell of non-Bravais lattices can lead to polarization-dependent properties such as chiral lattice resonances in square lattices with dimer unit cells<sup>34,35</sup> or the lattice Kerker effect in lattices of plasmonic trimer oligomers.<sup>36</sup> Expanding or shrinking the hexamer unit cells of a hexagonal lattice has also been shown to change the topological charge of the system and introduce polarization-tunable lasing.<sup>37</sup> Since non-Bravais lattices facilitate additional coupling interactions that affect near-field and far-field properties, understanding how lattice geometry responds to polarization is important.

Here we show the emergence of polarization-dependent features in the photonic band structure of plasmonic Kagome lattices with expanded unit cells. In Al NP lattices with reduced rotational symmetry, we observed SLR mode splitting at the K-points of the Kagome lattice as well as the emergence of an additional SLR band along the  $\Gamma$ -K directions under linear polarization. Excitation of this SLR band also depended on the direction of the circularly polarized light. Our calculations indicate that the chirality of the SLR band results from the excitation of inequivalent contributions of in-plane and out-of-plane dipolar NP excitations between left- and right-circularly polarized light. Engineering polarization-dependent features into the photonic dispersion diagram of non-Bravais NP lattices offers the potential for plasmonic systems to realize topological states.

## ■ RESULTS AND DISCUSSION

To design a plasmonic Kagome lattice responsive at visible wavelengths, we first calculated the band structure using the empty lattice approximation.  $^{31,38-40}$  Since SLRs result from hybridization of the LSPs of NPs to the diffractive modes of the lattice,  $^{38}$  we can estimate the dispersion properties based on periodicity. Geometrically, a Kagome lattice is a hexagonal lattice (lattice spacing,  $A_0$ ) with trimer unit cells (NP spacing,

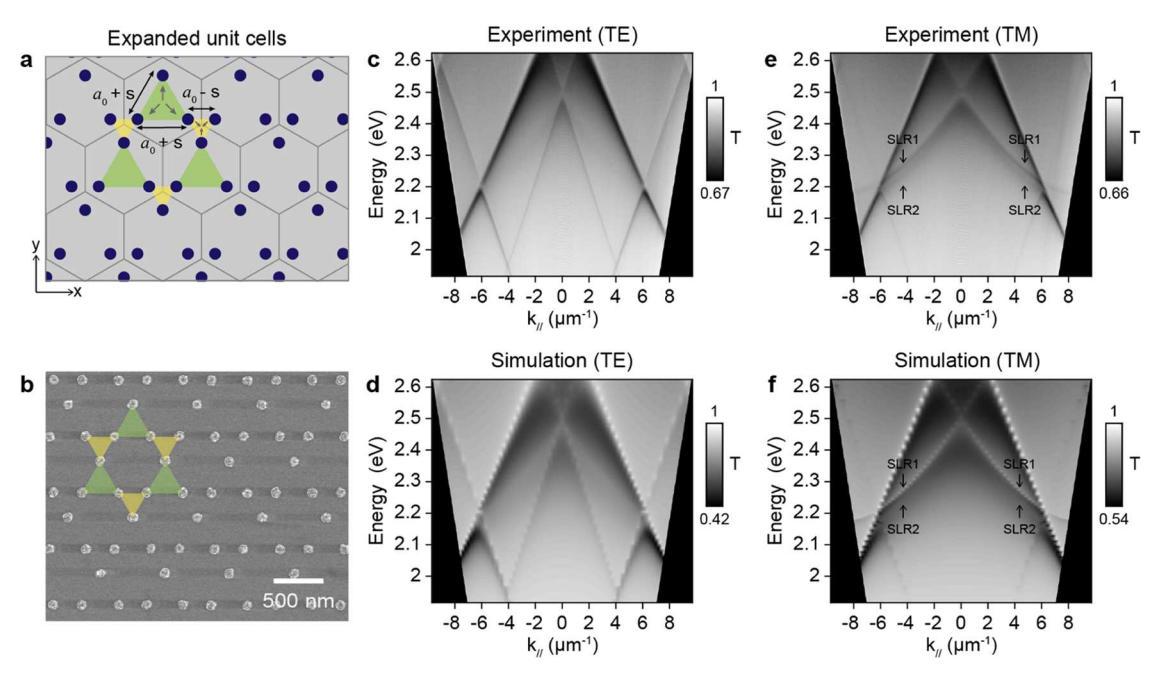


Figure 3. Photonic band structure of an Al Kagome lattice with expanded unit cells excited with linearly polarized light. (a) Scheme of the Kagome lattice with expanded unit cells ( $a_0$  + 40 nm). (b) SEM image of the fabricated Al Kagome lattice with expanded unit cells (Al NPs, d = 100 nm, h = 50 nm). Green triangles indicate the expanded trimer unit cells ( $a_0$  + 40 nm), and the yellow trimers indicate shrunken trimers in between the unit cells ( $a_0$  - 40 nm). (c) Measured and (d) simulated the optical band structure of a TE-polarized lattice along Γ-K. (e) Measured and (f) simulated optical band structure of a TM-polarized lattice along Γ-K.

 $a_0$ )<sup>40,41</sup> defined by three lattice vectors  $a_1$ ,  $a_2$ , and  $a_3$  (Figure 1a). Figure 1b summarizes the three-vector definition of the lattice, with the three-coordinate diffractive orders indicated by black, blue, and orange dots. The dispersion relation in the lattice plane is defined as  $E = \frac{\hbar c}{n} |k_{//} + G|$ , where E is the photon energy,  $\hbar$  is the reduced Planck's constant, c is the speed of light, n is the refractive index, G is the reciprocal lattice vector, and  $k_{//}$  is the in-plane wavevector. We identified that a hexagonal lattice with a spacing of  $A_0 = 680$  nm in a refractive index n = 1.45 environment produced K-points at the center of the visible spectrum. The K-points of the Kagome lattice were situated at the crossing of three degenerate sets of diffractive modes at wavevectors  $k_{//} \approx \pm 6.16 \, \mu \text{m}^{-1}$  and energy  $E = 2.22 \, \text{eV}$  (wavelength  $\lambda \approx 559 \, \text{nm}$  and incident angle  $\theta \approx \pm 33^\circ$  in air from the surface normal) (Figure 1c).

Figure 2a depicts a Kagome lattice (Al NP diameter d = 100nm, height h = 50 nm) with trimer unit-cell spacing  $a_0 = 340$ nm (blue triangles) and lattice spacing  $A_0 = 680$  nm on a quartz substrate; the rotational symmetry of the lattice is 6fold. Previous work demonstrated that the K-points of a plasmonic honeycomb lattice with 6-fold symmetry are located at the intersection of six diffractive modes. 42 Under transverse electric (TE)-polarization, the optical band structure shows Kpoints at the intersections of three sets of degenerate diffractive modes ( $k_{//} \approx \pm 6.1 \ \mu \text{m}^{-1}$ ,  $E \approx 2.2 \ \text{eV}$ ) (Figure 2b), in agreement with the diffraction-only model (Figure 1c). Under transverse magnetic (TM)-polarization, the K-points are at the same position in reciprocal space but are situated at the crossing between the (020)/(002) and  $(110)/(\overline{101})$  diffractive modes for  $\mathbf{k}_{//} < 0$  and the  $(0\overline{2}0)/(00\overline{2})$  and  $(\overline{11}0)/(10\overline{1})$ modes for  $k_{//} > 0$  (Figure 2c). Since the empty lattice approximation does not consider the effects of the NP material on the dispersion properties, we also carried out finitedifference time-domain (FDTD) simulations; neither the unit

cell nor NP material introduced additional features into the band structure (Figure S1). The calculated *K*-points are situated around ( $k_{//} \approx \pm 6.16~\mu \text{m}^{-1}$ ,  $E \approx 2.16~\text{eV}$ ), in agreement with experiment.

Since topological band gaps can be observed at the K-points of photonic Kagome lattices by shrinking or expanding unit-cell spacing  $(a_0)$  while keeping the lattice spacing  $(A_0)$  fixed, <sup>15,18,19</sup> we examined Al NP lattices with unit cells that were expanded by an amount s  $(a_0 + s)$  (Figure 3a, green triangles); the trimers in between the expanded unit cells were also shrunk by the same amount  $(a_0 - s)$  (Figure 3a, yellow triangles). Note that this change amounts to  $s/\sqrt{3}$  along the lattice vectors  $a_n$  (gray arrows). Although the unit-cell deformations maintain the 3-fold symmetry of the trimer, the mirror symmetry of the hexagonal lattice is now broken along the x-axis, and the rotational symmetry of the lattice is reduced from 6- to 3-fold.

We conducted a sweep from s = 0 to 100 nm to examine the effects of expanding the unit cells of a plasmonic Kagome lattice (Figure S2). Under TE-polarization, the undeformed lattice (s = 0 nm) exhibited a single SLR mode at the *K*-point. As the unit cells were expanded (s > 0), the SLR mode split into two, where the K1 mode increased in intensity and shifted to lower energies, while the K2 mode decreased in intensity and approached the Rayleigh anomaly. To determine how unit-cell changes affected the optical band structure experimentally, we fabricated an Al NP lattice with expanded trimer unit cells  $(a_0 + 40 \text{ nm}, \sim 23 \text{ nm along any lattice vector } a_n)$  on quartz (Figure 3b). We focused on the s = 40 nm deformation because the K1 and K2 modes were well-defined dips in the calculated transmission spectra at the K-point (Figure S2). Figure 3c shows that the TE-polarized band structure exhibited discontinuities around the *K*-points ( $k_{//} \approx \pm 6.1 \ \mu \text{m}^{-1}$ ,  $E \approx 2.2$ eV) that were not present in the unmodified lattice (Figure 2b). The simulated band structure showed that SLR bands

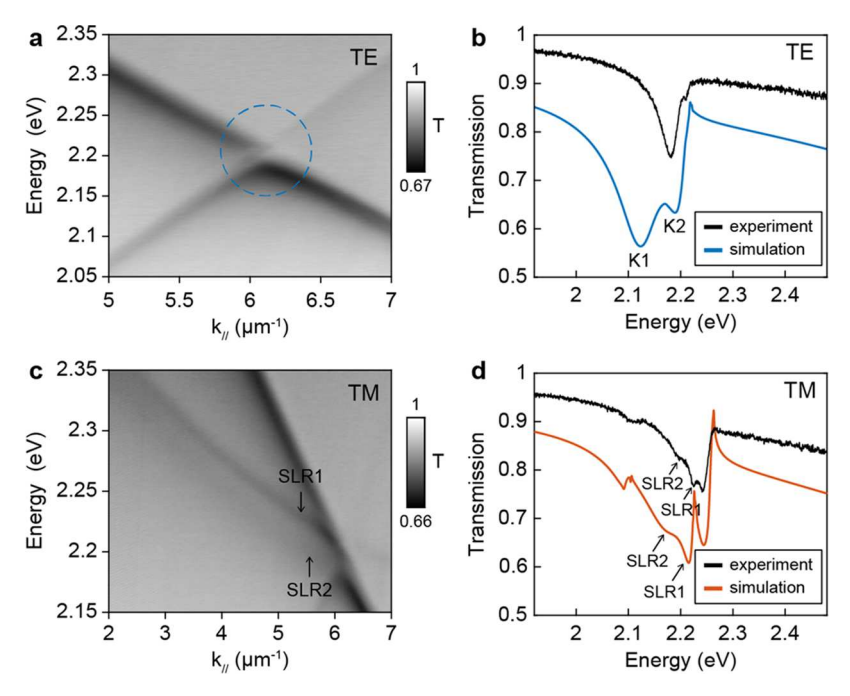


Figure 4. Mode splitting and emergence of additional SLR bands in the Al Kagome lattice with expanded unit cells. (a) Optical band structure of a fabricated Al Kagome lattice with expanded unit cells ( $a_0 + 40$  nm) under TE-polarization (Al NPs, d = 100 nm, h = 50 nm). K-point is circled in blue. (b) Measured and simulated transmission spectra at the K-point of the TE-polarized Kagome lattice ( $\theta \approx 33^{\circ}$ ). (c) Optical band structure of a fabricated Al Kagome lattice with expanded unit cells ( $a_0 + 40$  nm) under TM-polarization. (d) Measured and simulated transmission spectra of a TM-polarized Kagome lattice to the left of the K-point ( $\theta \approx 30^{\circ}$ ). The simulated transmission in panels (b) and (d) were shifted down to emphasize the features in the experimental data.

near the K-points ( $k_{//} \approx \pm 6.16 \, \mu \text{m}^{-1}$ ) shifted to lower energies compared to the Kagome lattice (Figure 3d). Under TMpolarization, an additional SLR band emerged below the (110)/(101) and (110)/(101) diffractive modes (Figure 3e). We assigned the SLR band that coincided with features in the unmodified Kagome lattice as SLR1 and the newly emergent band as SLR2. The calculated band structure showed features that were consistent with those of the new SLR band (Figure 3f). We also fabricated lattices with larger deformations (s =60, 80, and 100 nm) to examine trends in the unit-cell modifications (Figure S3). As the spacing of the trimer unit cells increased, the discontinuities at the K-point increased, which was consistent with the mode-splitting features observed at larger deformations in the FDTD simulations. The SLR2 band emerged in all of the samples where unit cells were expanded, which indicates that this band can be associated with the reduced symmetry of the lattice.

To examine the emergent features in detail, we analyzed the band structure around one of the K-points ( $k_{//} \approx 6.1 \ \mu \text{m}^{-1}$ ). Figure 4a shows a discontinuity ( $k_{//} \approx 6.1 \ \mu \text{m}^{-1}$ ,  $E \approx 2.2 \ \text{eV}$ ) (blue circle) under TE-polarization. We compared the measured transmission spectra at the K-point with FDTD calculations and found that the K1 and K2 modes were ca. 29 meV apart in experiment but ca. 66 meV apart in simulations (Figure 4b). This difference may be due to fabrication imperfections such as NP size (i.e., smaller NPs) and particle surface roughness, since NPs with nonuniform surfaces show lower transmission intensity compared to simulations. 43 In the undeformed Kagome lattice, the charge distribution plot of the SLR mode at the K-point shows that the NPs interact by inplane dipole coupling (Figure S4). In a lattice with expanded unit cells, the charge distribution plots of the K1 and K2 modes result from predominantly in-plane dipole coupling between the Al NPs but that in-plane quadrupole excitations also emerged as the trimers between neighboring unit cells shrank (Figure S5).

Under TM-polarization, a pair of SLR bands following the  $(\overline{110})/(\overline{101})$  diffractive modes of the lattice were observed (Figure 4c). The position of the SLR1 band was consistent with features in the unmodified Kagome lattice, while the SLR2 band was present only in a Kagome lattice with expanded unit cells. To understand how the SLR1 and SLR2 bands emerge in the modified lattice, we examined the transmission spectra where the two modes appeared as welldefined SLR dips, just to the left of the K-point ( $\theta \approx 30^{\circ}$ ,  $k_{SLR1}$  $\approx 5.47 \ \mu \mathrm{m}^{-1}$ ,  $k_{\mathrm{SLR2}} \approx 5.57 \ \mu \mathrm{m}^{-1}$ ). In calculations, the SLR1 mode is a narrow dip at higher energy than the broader SLR2 mode (Figure 4d, orange line). In the experiment, the two SLR modes were ca. 28 meV apart compared to 40 meV in simulations. The charge distribution plot of the single SLR mode (SLR1 in the modified lattice) in a Kagome lattice indicated coupling between the diffractive modes of the lattice to in-plane dipoles as well as hybridization between in-plane and out-of-plane dipole excitations in the NPs (Figure S6). Excitation of a Kagome lattice with TM-polarized light led to hybridization between in-plane dipole and out-of-plane dipole modes, which appeared as asymmetric surface charge distributions on Al NPs. 32 For lattices with expanded unit cells, the charge distribution plot of the SLR1 mode showed that the NPs exhibited both in-plane dipole coupling and hybridization between in-plane and out-of-plane dipoles (Figure S7). The charge distribution of SLR2 contained more NPs with hybridization between the in-plane and out-ofplane dipole modes, which suggests that out-of-plane dipole excitations primarily contribute to SLR2.

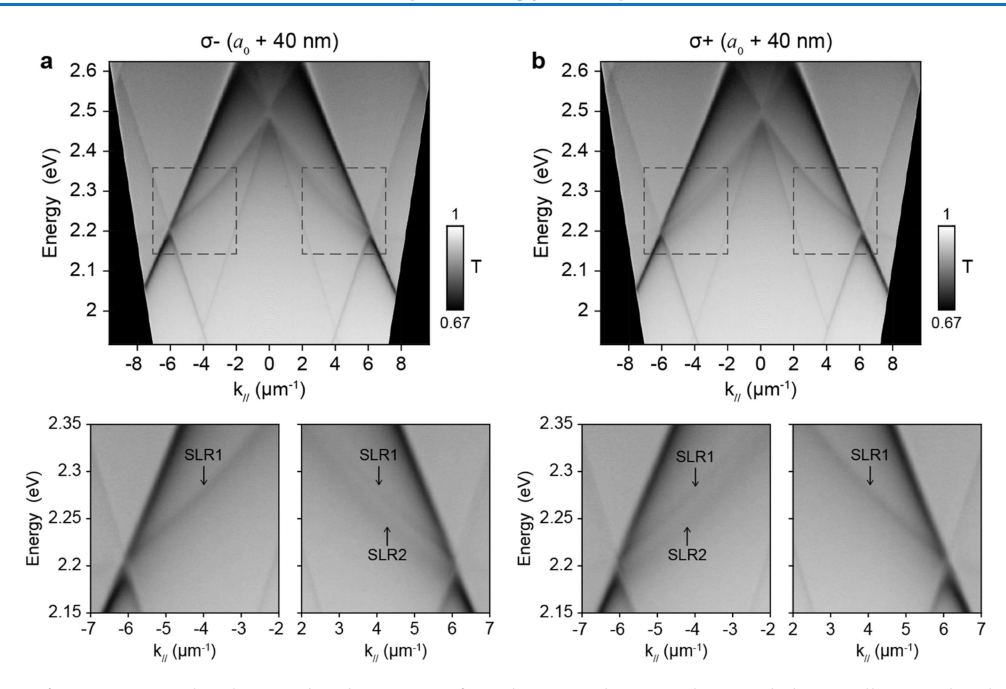


Figure 5. Emergence of asymmetry in the photonic band structure of an Al Kagome lattice with expanded unit cells excited with circularly polarized light. Measured optical band structure of a Kagome lattice with expanded unit cells ( $a_0 + 40$  nm) (Al NPS d = 100 nm, h = 50 nm) under (a)  $\sigma_-$  and (b)  $\sigma_+$  excitation. Measurements were taken along Γ-K. Zoom-ins highlight the chiral dependence of the parabolic bands in the band structure.

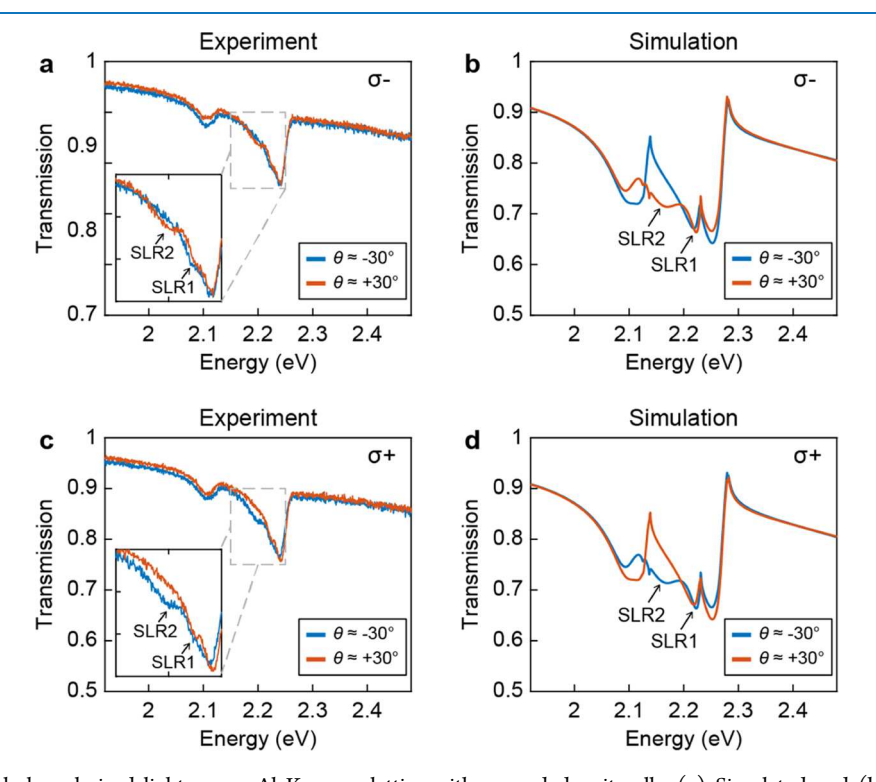


Figure 6. Effects of circularly polarized light on an Al Kagome lattice with expanded unit cells. (a) Simulated and (b) measured transmission spectra of a Kagome lattice with  $a_0$  + 40 nm unit-cell spacing under  $\sigma_-$  polarization. (c) Simulated and (d) measured transmission spectra of a Kagome lattice with  $a_0$  + 40 nm unit-cell spacing under  $\sigma_+$  polarization. Simulations and measurements were taken at  $\theta \approx -30^\circ$  (blue) and  $\theta \approx +30^\circ$  (orange) incidence angles in air.

Since expanding the trimer unit cells resulted in the emergence of additional SLR bands under linear polarization, we investigated whether the bands were also influenced by circularly polarized light. Under left circularly polarized light ( $\sigma_{-}$ ), the band structure exhibited asymmetric properties (Figure 5a). At  $k_{//} < 0$ , only the SLR1 band was present in the band structure, but both SLR1 and SLR2 bands were observed

when  $k_{//} > 0$ . These asymmetric features were confirmed in the FDTD simulations (Figure S8). Under the right-circularly polarized light  $(\sigma_+)$ , the opposite response was observed (Figure Sb). At  $k_{//} < 0$ , the SLR1 and SLR2 bands were present, while only the SLR1 band emerged at  $k_{//} > 0$ , in agreement with FDTD simulations (Figure S8). As a control, we measured the unmodified Kagome lattice under circularly

polarized light and found no asymmetric features (Figure S9). The data suggest that the SLR2 mode associated with plasmonic Kagome lattices having expanded unit cells is chiral since its presence depends on the helicity of the incident light source.

To confirm the chirality of the SLR2 mode, we compared the band structure asymmetry under different circular polarization conditions at different incident angles. Under  $\sigma_{-}$ excitation and  $\theta \approx -30^{\circ}$ , we confirmed the presence of only the SLR1 mode in the experimental spectra, while both SLR1 and SLR2 modes appeared at  $\theta \approx +30^{\circ}$  (Figure 6a). The simulated transmission spectra confirmed that the SLR2 mode emerged at  $\theta \approx +30^{\circ}$ , but the mode could not be identified at  $\theta$  $\approx -30^{\circ}$ . The data indicates that the transmission of the SLR2 band at  $k_{//}$  < 0 is affected by  $\sigma_{-}$  excitation. We calculated the charge distribution at  $\theta \approx \pm 30^\circ$  to examine the coupling mechanisms of the SLR1 and SLR2 modes. The charge distribution plot of SLR1 at  $\theta \approx -30^{\circ}$  indicates that the mode is from the excitation of both the in-plane dipole and hybridized in-plane dipole and out-of-plane dipole modes in the NPs (Figure S10). At  $\theta \approx +30^{\circ}$ , the SLR1 and SLR2 modes have NPs with in-plane dipole and hybridized dipole excitations. Under  $\sigma_+$  excitation, we observed the opposite behavior: the SLR1 and SLR2 modes both appeared at  $\theta \approx$  $-30^{\circ}$ , while only SLR1 was observed at  $\theta \approx +30^{\circ}$  (Figure 6c). FDTD simulations confirmed that the SLR2 mode was only present at  $\theta$  < 0° ( $k_{//}$  < 0) (Figure 6d). The charge distribution plots of the SLR1 and SLR2 modes at  $\theta \approx -30^{\circ}$ indicated that the two modes resulted from in-plane dipole excitations as well as hybridization between in-plane dipole and out-of-plane dipole modes of the NPs (Figure S11). At  $\theta \approx$ +30°, the charge plot for SLR1 had in-plane dipole and hybridized dipole mode coupling between neighboring NPs. Although the emergence of the SLR2 mode depended on the helicity of the incident light, both SLR1 and SLR2 showed similar surface charge distributions; based only on the charge distribution calculations, the mechanism of the chiral response of the SLR2 mode could not be determined.

Therefore, for more insight, we calculated the in-plane and out-of-plane quasi-normal modes (QNMs) of the unmodified and deformed (expanded) Kagome lattices using the coupled dipole method. 38,44 In this approach, the fully retarded and frequency-dependent electric field of each LSP dipole mediates the coupling between all of the NPs in the system, leading to a nonlinear eigenvalue problem governing the QNMs. We used 12 NPs as a reducible unit cell for the calculations because this was the smallest arrangement that could account for the reduction of rotational symmetry in the lattice as the NP trimers are expanded/shrunken (Figure S12). After determining the QNMs, the reducible unit cell was excited with  $\sigma_+$  light at  $\theta = \pm 20^{\circ}$  in an n = 1.45 environment ( $\theta \approx 30^{\circ}$  in air), and the driven states  $|d_{ind}\rangle$  were projected onto the QNM basis {|  $QNM_n >$ , resulting in 16 nondegenerate in-plane QNMs. In the unmodified Kagome reducible unit cell,  $\sigma_+$  excitation resulted in the same combination of QNMs at  $\theta = \pm 20^{\circ}$ (Figure S13). In contrast, in the deformed Kagome reducible unit cell, the  $\sigma_+$  excitation field drove a different superposition of QNMs at  $\theta = +20^{\circ}$  and  $\theta = -20^{\circ}$ . We also calculated eight nondegenerate out-of-plane QNMs and observed a similar trend for differences between the unmodified and deformed unit cells (Figure S14). The calculations suggest that the chiral response of the SLR2 mode was from different contributions of in-plane and out-of-plane dipole modes. Since the SLR2 mode

was only present at  $\theta = -20^{\circ}$  ( $\theta \approx -30^{\circ}$  in air) under  $\sigma_+$  excitation (Figure 6), the in-plane dipoles were the dominant contributors to the chirality of SLR2 because they had greater  $|\langle \text{QNM}_n|d_{\text{ind}}\rangle|$  values at  $\theta = -20^{\circ}$  compared to the out-of-plane modes. No asymmetry was observed in the band structure of the unmodified Kagome reducible unit cell because the superpositions of the QNMs were independent of the incident angle.

To determine how QNM mixing changes the spectral responses of the reducible unit cell and a finite Kagome lattice, we calculated the extinction spectra and their angular scattering profiles under  $\sigma_+$  light (Figure S15). The extinction spectra of the expanded reducible unit cell showed a small chiral response at  $\sim$ 4.13 eV, and a finite lattice (17  $\mu$ m  $\times$  15  $\mu$ m) with expanded unit cells showed a chiral response around 2.2 eV that was consistent with the appearance of the SLR2 mode at  $\theta = -20^{\circ}$  ( $\theta \approx -30^{\circ}$  in air) in FDTD simulations and experiments (Figure 6). A chiral response was also observed from the expanded reducible unit cell under  $\sigma_-$  excitation at  $\theta$ =  $\pm 20^{\circ}$  (Figure S16). The unmodified reducible unit cell and Kagome lattice exhibited identical extinction spectra at  $\theta$  = ±20°, indicating a lack of chirality. In addition, the angular scattering profiles of the unmodified reducible unit cell were symmetric, as expected (Figure S16). This property will remain even when the unit cell is tiled into a lattice through a lattice structure factor.<sup>36</sup> In contrast, the angular scattering profiles of the expanded reducible unit cell were asymmetric and representative of a chiral response that should also be maintained when the cell was scaled into a lattice.

## CONCLUSIONS

In summary, we demonstrated that Al NP Kagome lattices with expanded unit cells exhibit polarization-dependent dispersion properties. Under linearly polarized light, mode splitting at the K-point was observed under TE-polarization, while an additional SLR band emerged along the  $\Gamma$ -K direction under TM-polarization. The chiral response of the emergent SLR mode was dependent on the direction of circularly polarized light. Calculations indicate that the observed chirality results from different contributions from in-plane and out-of-plane LSP dipole modes to the formation of the SLR mode, producing asymmetries in the angular scattering profiles and associated momentum resolved spectra. This work demonstrates how lattice engineering of a non-Bravais unit cell can tune the near-field and far-field properties of a lattice by reducing its rotational symmetry. The results provide opportunities to establish design rules for introducing topological states into plasmonic systems in the visible regime.

# METHODS

Fabrication of Al NP Lattices. We patterned the Al NP lattices on quartz substrates using electron-beam lithography (EBL, Raith Voyager 100). First, we spin-coated a thin layer of the PMMA A2 photoresist onto a quartz substrate. We then used thermal evaporation to deposit a 7 nm thick Au layer onto the quartz to minimize charging effects that can occur when patterning on an insulating substrate. We patterned lattices onto the photoresist using EBL and developed the pattern in a 1:3 solution of MIBK:IPA (methyl isobutyl ketone: isopropanol) to create a nanohole photoresist mask. Al was deposited through the photoresist mask using electron-beam evaporation, and acetone was used to lift off the photoresist.

FDTD Simulations. Finite-difference time-domain (FDTD) simulations (Ansys-Lumerical) were used to calculate the linear optical properties of the Al NP lattices. The optical constants for Al used in the simulations were taken from the Palik handbook. 45 To construct the optical dispersion diagrams and calculate the near-field interactions of the Kagome lattices under linear polarization (TE, TM), we used the BFAST plane wave source to calculate the transmission of the lattices at varying incident angles along the  $\Gamma$ -K direction. To simulate circularly polarized light, we used two plane wave sources: the first source had the electric field polarized along the x-axis, and the second source was polarized along the y-axis with a phase change applied to the second source. We defined simulations with a  $-\frac{\pi}{2}$  phase change as  $\sigma_{-}$  and simulations with a  $+\frac{\pi}{2}$  phase change as  $\sigma_+$ . A uniform mesh of 4 nm (x,y,z) was placed around the NPs in the simulations to improve the accuracy of the calculated electromagnetic fields. To convert the simulated data from wavelength ( $\lambda$ )-incident angle ( $\theta$ ) to energy (E)-inplane wavevector  $(k_{//})$ , we used the following equations: E = $hc/\lambda$  and  $k_{//} = (2\pi n/\lambda)\sin\theta$ , where h is Planck's constant and c is the speed light. The dispersion properties were converted from a quartz to air environment (n = 1) since measurements were taken in air.

Photonic Band Structure Measurements. The photonic band structures of the lattices were measured using a Fourier microscopy setup. 46 We imaged the back focal plane of a 20× Plan Apo objective lens (Nikon Japan, NA = 0.75) onto the entrance slit of a SP2500 spectrometer (Teledyne Princeton Instruments). The objective lens can collect light emitted from the sample within a range of  $\theta \approx \pm 48^{\circ}$ . The angle  $(\theta)$  and wavelength ( $\lambda$ ) resolved image was captured by a CCD camera (PIXIS 400, Teledyne Princeton Instruments). To convert the measured data from wavelength ( $\lambda$ )-incident angle ( $\theta$ ) to energy (*E*)-momentum ( $\mathbf{k}_{//}$ ), we used the following equations:  $E = hc/\lambda$  and  $k_{//} = (2\pi n/\lambda)\sin\theta$ , where h is Planck's constant and c is the speed light. We produced circularly polarized light using a linear polarizer and a quarter-wave plate. To create a uniform refractive index environment around the NP lattice for the measurements, we placed a drop of immersion oil (n =1.45) over the lattice and used a quartz coverslip to cap the oil

Lattice Extinction Calculations. In the coupled dipole method, 36,44,47 the induced polarization of each Al NP is modeled as a point electric dipole Pi. In matrix form, the coupled dipole equations for an N particle\_system can be organized into the linear system of equations,  $A(\omega)P(\omega) = E_0$ , where the  $3N \times 3N$  coupling matrix  $A(\omega)$  consists of  $3 \times 3$ matrix blocks  $A_{ij}(\omega) = \vec{\alpha}^{-1}(\omega)\delta_{ij} - (k^2/\varepsilon)G_{ij}(\omega)$  connecting dipoles i and j. The anisotropic dipole polarizability  $\vec{\alpha}$ describing each NP is determined based on the l = 1 electric Mie coefficient, with in-plane and out-of-plane polarizability components corresponding to 100 and 50 nm diameter Al spheres, respectively. The frequency-dependent bulk optical constants from Blaber et al. 48 were used to evaluate these polarizability components. The purely off-diagonal interaction matrix blocks  $G_{ij}(\omega) = G(\mathbf{r}_{ij}, \mathbf{r}_{jj}, \text{ and } \omega)(1 - \delta_{ij})$  account for dipole-dipole coupling with  $k = \omega \sqrt{\varepsilon}/c$  and background refractive index  $\sqrt{\varepsilon}$ .  $P(\omega)$  and  $E_0(\omega)$  are  $3N \times 1$  column vectors containing the Cartesian components of N induced dipole moments  $\mathbf{P}_i(\omega)$  and excitation fields  $\mathbf{E}_0(\mathbf{r}_i, \omega)$  with  $\hat{\boldsymbol{\epsilon}}$ polarization direction. The per unit-cell extinction cross section,  $\sigma_{\rm ext}(\omega)$ , is determined by assessing the imaginary

component of the specific lattice response's tensor element, which is aligned with the direction of polarization of the incident field,  $\sigma_{\rm ext}(\omega) = (4\pi k/\sqrt{\varepsilon}) {\rm Im}\{\hat{e}\cdot \vec{\bf A}^{-1}\cdot \hat{e}\}.$ 

Scattering Angular Distribution Calculations. Differential scattering angular distributions were calculated by evaluating  $E(\mathbf{r})$  and  $H(\mathbf{r})$  within the dipole approximation at discrete sets of points that were arranged around the perimeter of a circle and centered at a target position. The circle had a radius that was  $\sim 10\times$  the excitation wavelength. The time-averaged power scattered into direction  $\hat{\mathbf{n}}$  is  $dP/d\Omega = c/8\pi Re\{r^2\hat{\mathbf{n}}\cdot[E(\mathbf{r})\times H^*(\mathbf{r})]\}$  where  $E(\mathbf{r})$  and  $H(\mathbf{r})$  are the total scattered electric and magnetic fields (i.e., summed over dipole sources comprising the target) at the observation point and  $\mathbf{r}=r\hat{\mathbf{n}}$ .

Complex Quasi-Normal Modes Calculations. The quasi-normal modes of the reducible unit cells were calculated using the coupled dipole method. 44 In this approach, the complex-valued eigenfrequencies of the 12-NP reducible unit cell were determined by the condition  $\det A(\omega_r) = 0$  for the eigenvalue problem  $\mathbf{A}(\omega)\mathbf{P}(\omega) = 0$ , where  $\mathbf{A}(\omega)$  consists of 3 × 3 matrix blocks  $\hat{A}_{ij}(\omega) = \vec{\alpha}^{-1}(\omega)\delta_{ij} - (k^2/\varepsilon)\hat{G}_{ij}(\omega)$ connecting dipoles i and j. The system possesses an eigenvalue  $\alpha^{-1}(\omega_r)$  for complex-valued frequency  $\omega_r$  when  $|\det \mathbf{A}(\omega_r)| = 0$ . A numerical search for the complex-valued eigenfrequencies  $\omega_r$ was performed by seeking the minima of the nonlinear  $|\det \mathbf{A}(\omega_r)|$  surface using a grid search over finite domains in real and imaginary frequency space. Once the eigenfrequencies  $\omega_r$  were found, we constructed and numerically diagonalized the  $G(\omega)$  matrix to obtain a new set of eigenvalues  $\lambda_n$ . The eigenvector  $P_r(\omega_r)$  was selected based on the numerically determined eigenvalue  $\lambda_n$  closest to  $\alpha^{-1}(\omega_r)$ .

## ASSOCIATED CONTENT

#### Supporting Information

The Supporting Information is available free of charge at https://pubs.acs.org/doi/10.1021/acsphotonics.3c01518.

FDTD simulated band structures of an Al Kagome lattice under linear polarization; mode splitting at the K-point of deformed Al Kagome lattices; near-field interactions at the K-point of a TE-polarized deformed Al Kagome lattice; near-field interactions at the K-point of a TM-polarized deformed Al Kagome lattice; FDTD simulated band structures of a circularly polarized deformed Al Kagome lattice; measured band structures of a circularly polarized undeformed Al Kagome lattice; near-field interactions in a  $(\sigma_-)$ -polarized Al Kagome lattice with expanded unit cells; near-field interactions in a  $(\sigma_+)$ -polarized Al Kagome lattice with expanded unit cells; in-plane and out-of-plane eigenmode contributions to SLR formation; and optical extinction spectra and scattering angular distribution (PDF)

# AUTHOR INFORMATION

## **Corresponding Author**

Teri W. Odom — Department of Materials Science and Engineering, Northwestern University, Evanston, Illinois 60208, United States; Department of Chemistry and Graduate Program in Applied Physics, Northwestern University, Evanston, Illinois 60208, United States; orcid.org/0000-0002-8490-292X; Email: todom@northwestern.edu

#### **Authors**

Xitlali G. Juarez – Department of Materials Science and Engineering, Northwestern University, Evanston, Illinois 60208, United States; oorcid.org/0000-0002-4742-3110

Francisco Freire-Fernández — Department of Chemistry, Northwestern University, Evanston, Illinois 60208, United States; © orcid.org/0000-0002-6539-419X

Siamak Khorasani — Department of Materials Science and Engineering, University of Washington, Seattle, Washington 98195, United States; oorcid.org/0000-0003-4395-6910

Marc R. Bourgeois – Department of Chemistry, University of Washington, Seattle, Washington 98195, United States

Yi Wang — Graduate Program in Applied Physics, Northwestern University, Evanston, Illinois 60208, United States; © orcid.org/0000-0002-9509-7962

David J. Masiello — Department of Materials Science and Engineering, University of Washington, Seattle, Washington 98195, United States; Department of Chemistry, University of Washington, Seattle, Washington 98195, United States; orcid.org/0000-0002-1187-0920

George C. Schatz – Department of Chemistry, Northwestern University, Evanston, Illinois 60208, United States; orcid.org/0000-0001-5837-4740

Complete contact information is available at: https://pubs.acs.org/10.1021/acsphotonics.3c01518

#### **Notes**

The authors declare no competing financial interest.

# ACKNOWLEDGMENTS

This work was supported by the National Science Foundation (NSF) under DMR-1904385 and DMR-2207215 (X.G.J., G.C.S., and T.W.O.) and the Vannevar Bush Faculty Fellowship from the Department of Defense (DoD) under N00014-17-1-3023 (F.F.-F. and T.W.O). Work at the University of Washington was supported by NSF under CHE-2118333 and QII-TAQS-1936100 (S.K., M.R.B., D.J.M.). This work used the Northwestern University Micro/ Nano Fabrication Facility (NUFAB) and EPIC facility of Northwestern University's NUANCE Center, which are supported by the Soft and Hybrid Nanotechnology Experimental (SHyNE) Resource (NSF ECCS-2025633), the International Institute for Nanotechnology (IIN), Northwestern's Materials Research Science and Engineering Center (MRSEC) (NSF DMR-1720139), and the MRI (NSF DMR-1828676). This research was supported in part by the Quest high-performance computing facility at Northwestern University, which is jointly supported by the Office of the Provost, the Office for Research, and Northwestern University Information Technology.

## REFERENCES

- (1) Lu, L.; Joannopoulos, J. D.; Soljačić, M. Topological photonics. *Nat. Photonics* **2014**, *8* (11), 821–829.
- (2) Khanikaev, A. B.; Shvets, G. Two-dimensional topological photonics. *Nat. Photonics* **2017**, *11* (12), 763–773.
- (3) Ozawa, T.; Price, H. M.; Amo, A.; Goldman, N.; Hafezi, M.; Lu, L.; Rechtsman, M. C.; Schuster, D.; Simon, J.; Zilberberg, O.; Carusotto, I. Topological photonics. *Rev. Mod. Phys.* **2019**, 91 (1), No. 015006.
- (4) Wang, Z.; Chong, Y.; Joannopoulos, J. D.; Soljačić, M. Observation of unidirectional backscattering-immune topological electromagnetic states. *Nature* **2009**, *461* (7265), 772–775.

- (5) Wu, L.-H.; Hu, X. Scheme for Achieving a Topological Photonic Crystal by Using Dielectric Material. *Phys. Rev. Lett.* **2015**, *114* (22), No. 223901.
- (6) Amo, A. When quantum optics meets topology. Science 2018, 359 (6376), 638-639.
- (7) Liu, W.; Hwang, M.; Ji, Z.; Wang, Y.; Modi, G.; Agarwal, R. Z2 Photonic Topological Insulators in the Visible Wavelength Range for Robust Nanoscale Photonics. *Nano Lett.* **2020**, 20 (2), 1329–1335.
- (8) Barik, S.; Karasahin, A.; Flower, C.; Cai, T.; Miyake, H.; DeGottardi, W.; Hafezi, M.; Waks, E. A topological quantum optics interface. *Science* **2018**, 359 (6376), 666–668.
- (9) Liu, W.; Ji, Z.; Wang, Y.; Modi, G.; Hwang, M.; Zheng, B.; Sorger, V. J.; Pan, A.; Agarwal, R. Generation of helical topological exciton-polaritons. *Science* **2020**, *370* (6516), 600–604.
- (10) Guddala, S.; Komissarenko, F.; Kiriushechkina, S.; Vakulenko, A.; Li, M.; Menon, V. M.; Alù, A.; Khanikaev, A. B. Topological phonon-polariton funneling in midinfrared metasurfaces. *Science* **2021**, *374* (6564), 225–227.
- (11) Yang, L.; Li, G.; Gao, X.; Lu, L. Topological-cavity surface-emitting laser. *Nat. Photonics* **2022**, *16* (4), 279–283.
- (12) Shao, Z.-K.; Chen, H.-Z.; Wang, S.; Mao, X.-R.; Yang, Z.-Q.; Wang, S.-L.; Wang, X.-X.; Hu, X.; Ma, R.-M. A high-performance topological bulk laser based on band-inversion-induced reflection. *Nat. Nanotechnol.* **2020**, *15* (1), 67–72.
- (13) Ezawa, M. Higher-Order Topological Insulators and Semimetals on the Breathing Kagome and Pyrochlore Lattices. *Phys. Rev. Lett.* **2018**, *120* (2), No. 026801.
- (14) Zhang, Y.; Wu, R. P. H.; Shi, L.; Fung, K. H. Second-Order Topological Photonic Modes in Dipolar Arrays. *ACS Photonics* **2020**, 7 (8), 2002–2009.
- (15) Li, M.; Zhirihin, D.; Gorlach, M.; Ni, X.; Filonov, D.; Slobozhanyuk, A.; Alù, A.; Khanikaev, A. B. Higher-order topological states in photonic kagome crystals with long-range interactions. *Nat. Photonics* **2020**, *14* (2), 89–94.
- (16) Ni, X.; Weiner, M.; Alù, A.; Khanikaev, A. B. Observation of higher-order topological acoustic states protected by generalized chiral symmetry. *Nat. Mater.* **2019**, *18* (2), 113–120.
- (17) Gong, Y.; Wong, S.; Bennett, A. J.; Huffaker, D. L.; Oh, S. S. Topological Insulator Laser Using Valley-Hall Photonic Crystals. *ACS Photonics* **2020**, *7* (8), 2089–2097.
- (18) Vakulenko, A.; Kiriushechkina, S.; Wang, M.; Li, M.; Zhirihin, D.; Ni, X.; Guddala, S.; Korobkin, D.; Alù, A.; Khanikaev, A. B. Near-Field Characterization of Higher-Order Topological Photonic States at Optical Frequencies. *Adv. Mater.* **2021**, *33* (18), No. 2004376.
- (19) Vakulenko, A.; Kiriushechkina, S.; Smirnova, D.; Guddala, S.; Komissarenko, F.; Alù, A.; Allen, M.; Allen, J.; Khanikaev, A. B. Adiabatic topological photonic interfaces. *Nat. Commun.* **2023**, *14* (1), No. 4629.
- (20) Berestennikov, A.; Kiriushechkina, S.; Vakulenko, A.; Pushkarev, A. P.; Khanikaev, A. B.; Makarov, S. V. Perovskite Microlaser Integration with Metasurface Supporting Topological Waveguiding. ACS Nano 2023, 17 (5), 4445–4452.
- (21) Peng, S.; Schilder, N. J.; Ni, X.; van de Groep, J.; Brongersma, M. L.; Alù, A.; Khanikaev, A. B.; Atwater, H. A.; Polman, A. Probing the Band Structure of Topological Silicon Photonic Lattices in the Visible Spectrum. *Phys. Rev. Lett.* **2019**, *122* (11), No. 117401.
- (22) Zou, S.; Janel, N.; Schatz, G. C. Silver nanoparticle array structures that produce remarkably narrow plasmon lineshapes. *J. Chem. Phys.* **2004**, *120* (23), 10871–10875.
- (23) Wang, D.; Guan, J.; Hu, J.; Bourgeois, M. R.; Odom, T. W. Manipulating Light-Matter Interactions in Plasmonic Nanoparticle Lattices. *Acc. Chem. Res.* **2019**, *52* (11), 2997–3007.
- (24) Kravets, V. G.; Kabashin, A. V.; Barnes, W. L.; Grigorenko, A. N. Plasmonic Surface Lattice Resonances: A Review of Properties and Applications. *Chem. Rev.* **2018**. *118* (12), 5912–5951.
- (25) Proctor, M.; Paz, M. B. d.; Bercioux, D.; García-Etxarri, A.; Huidobro, P. A. Higher-order topology in plasmonic Kagome lattices. *Appl. Phys. Lett.* **2021**, *118* (9), No. 091105.

- (26) Proctor, M.; Huidobro, P. A.; Maier, S. A.; Craster, R. V.; Makwana, M. P. Manipulating topological valley modes in plasmonic metasurfaces. *Nanophotonics* **2020**, *9* (3), 657–665.
- (27) Proctor, M.; Craster, R. V.; Maier, S. A.; Giannini, V.; Huidobro, P. A. Exciting Pseudospin-Dependent Edge States in Plasmonic Metasurfaces. *ACS Photonics* **2019**, *6* (11), 2985–2995.
- (28) Pocock, S. R.; Xiao, X.; Huidobro, P. A.; Giannini, V. Topological Plasmonic Chain with Retardation and Radiative Effects. *ACS Photonics* **2018**, 5 (6), 2271–2279.
- (29) Honari-Latifpour, M.; Yousefi, L. Topological plasmonic edge states in a planar array of metallic nanoparticles. *Nanophotonics* **2019**, 8 (5), 799–806.
- (30) Humphrey, A. D.; Barnes, W. L. Plasmonic surface lattice resonances on arrays of different lattice symmetry. *Phys. Rev. B* **2014**, 90 (7), No. 075404.
- (31) Guo, R.; Hakala, T. K.; Törmä, P. Geometry dependence of surface lattice resonances in plasmonic nanoparticle arrays. *Phys. Rev. B* **2017**, 95 (15), No. 155423.
- (32) Li, R.; Bourgeois, M. R.; Cherqui, C.; Guan, J.; Wang, D.; Hu, J.; Schaller, R. D.; Schatz, G. C.; Odom, T. W. Hierarchical Hybridization in Plasmonic Honeycomb Lattices. *Nano Lett.* **2019**, 19 (9), 6435–6441.
- (33) Baur, S.; Sanders, S.; Manjavacas, A. Hybridization of Lattice Resonances. ACS Nano 2018, 12 (2), 1618–1629.
- (34) Cotrufo, M.; Osorio, C. I.; Koenderink, A. F. Spin-Dependent Emission from Arrays of Planar Chiral Nanoantennas Due to Lattice and Localized Plasmon Resonances. *ACS Nano* **2016**, *10* (3), 3389–3397.
- (35) Cerdán, L.; Zundel, L.; Manjavacas, A. Chiral Lattice Resonances in 2.5-Dimensional Periodic Arrays with Achiral Unit Cells. *ACS Photonics* **2023**, *10* (6), 1925–1935.
- (36) Bourgeois, M. R.; Rossi, A. W.; Chalifour, M.; Cherqui, C.; Masiello, D. J. Lattice Kerker Effect with Plasmonic Oligomers. *J. Phys. Chem. C* **2021**, *125* (34), 18817–18826.
- (37) Salerno, G.; Heilmann, R.; Arjas, K.; Aronen, K.; Martikainen, J.-P.; Törmä, P. Loss-Driven Topological Transitions in Lasing. *Phys. Rev. Lett.* **2022**, *129* (17), No. 173901.
- (38) Cherqui, C.; Bourgeois, M. R.; Wang, D.; Schatz, G. C. Plasmonic Surface Lattice Resonances: Theory and Computation. *Acc. Chem. Res.* **2019**, 52 (9), 2548–2558.
- (39) Guan, J.; Bourgeois, M. R.; Li, R.; Hu, J.; Schaller, R. D.; Schatz, G. C.; Odom, T. W. Identification of Brillouin Zones by In-Plane Lasing from Light-Cone Surface Lattice Resonances. *ACS Nano* **2021**, *15* (3), 5567–5573.
- (40) Yang, A.; Hryn, A. J.; Bourgeois, M. R.; Lee, W.-K.; Hu, J.; Schatz, G. C.; Odom, T. W. Programmable and reversible plasmon mode engineering. *Proc. Natl. Acad. Sci. U.S.A.* **2016**, *113* (50), 14201–14206.
- (41) Juarez, X. G.; Li, R.; Guan, J.; Reese, T.; Schaller, R. D.; Odom, T. W. M-Point Lasing in Hexagonal and Honeycomb Plasmonic Lattices. *ACS Photonics* **2022**, *9* (1), 52–58.
- (42) Guo, R.; Nečada, M.; Hakala, T. K.; Väkeväinen, A. I.; Törmä, P. Lasing at K Points of a Honeycomb Plasmonic Lattice. *Phys. Rev. Lett.* **2019**, 122 (1), No. 013901.
- (43) Deng, S.; Li, R.; Park, J.-E.; Guan, J.; Choo, P.; Hu, J.; Smeets, P. J. M.; Odom, T. W. Ultranarrow plasmon resonances from annealed nanoparticle lattices. *Proc. Natl. Acad. Sci. U.S.A.* **2020**, *117* (38), 23380–23384.
- (44) Bourgeois, M. R.; Rossi, A. W.; Khorasani, S.; Masiello, D. J. Optical Control over Thermal Distributions in Topologically Trivial and Non-Trivial Plasmon Lattices. *ACS Photonics* **2022**, *9* (11), 3656–3667.
- (45) Palik, E. D.; Ghosh, G. Handbook of Optical Constants of Solids: Vol. 2; Elsevier Science, 1991.
- (46) Kurvits, J. A.; Jiang, M.; Zia, R. Comparative analysis of imaging configurations and objectives for Fourier microscopy. *J. Opt. Soc. Am.* A **2015**, 32 (11), 2082–2092.

- (47) Purcell, E. M.; Pennypacker, C. R. Scattering and Absorption of Light by Nonspherical Dielectric Grains. *Astrophys. J.* **1973**, *186*, 705–714.
- (48) Blaber, M. G.; Arnold, M. D.; Ford, M. J. Search for the Ideal Plasmonic Nanoshell: The Effects of Surface Scattering and Alternatives to Gold and Silver. *J. Phys. Chem. C* **2009**, *113* (8), 3041–3045.